ACS NANOSCIENCE Au
AN OPEN ACCESS JOURNAL OF THE AMERICAN CHEMICAL SOCIETY

pubs.acs.org/nanoau
Article

Crystal Facet Regulation and Ru Incorporation of Co_3O_4 for Acidic Oxygen Evolution Reaction Electrocatalysis

Published as part of ACS Nanoscience Au special issue "Advances in Energy Conversion and Storage at the Nanoscale".

Mengting Zhao and Hanfeng Liang*

Cite This: *ACS Nanosci. Au* 2024, 4, 409–415
Read Online

ACCESS | Metrics & More | Article Recommendations | Supporting Information

ABSTRACT: Acidic oxygen evolution reaction (OER) has long been the bottleneck of proton exchange membrane water electrolysis. Ru- and Ir-based oxides are currently state-of-the-art electrocatalysts for acidic OER, but their high cost limits their widespread application. Co_3O_4 is a promising alternative, yet the performance requires further improvement. Crystal facet engineering can effectively regulate the kinetics of surface electrochemistry and thus enhance the OER performance. However, the facet-dependent OER activity and corrosion behavior of Co_3O_4 have not been thoroughly studied. In this study, we systematically investigated the OER performance and crystal facet dependency of Co_3O_4. The results demonstrate that Co_3O_4 with mixed {111} and {110} facets exhibits better OER activity and stability than Co_3O_4 with {111} or {100} facets. The surface Co^{3+} species are responsible for the high OER activity, but its transformation to CoO_2 is also the root cause of the dissolution, leading to an activity−stability trade-off effect. The possible approach to addressing this issue would be to increase the Co^{3+} contents by nanostructure engineering. To further improve the performance, Ru is introduced to the best-performing Co_3O_4. The resulting Co_3O_4/RuO_2 heterostructure exhibits an overpotential of 257 mV at 10 mA cm^{-2} and can stably catalyze the OER for 100 h.

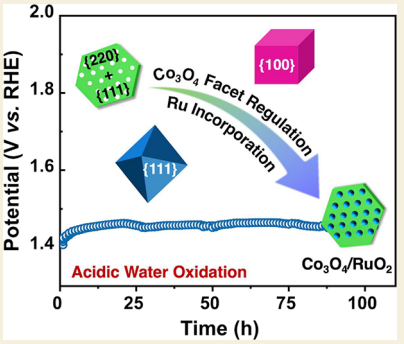

KEYWORDS: *acidic OER, Co_3O_4, crystal facets, RuO_2, heterostructure*

1. INTRODUCTION

Proton exchange membrane (PEM) water electrolysis is recognized a sustainable avenue for hydrogen production.[1] Within this process, the oxygen evolution reaction (OER) is the kinetically slower yet crucial step that significantly influences the overall energy efficiency. The corrosive nature of the acidic environment of PEM electrolyzers presents additional challenges in catalyst selection and design.[2,3] Currently noble-metal-based compounds such as IrO_2, RuO_2, and their derivates are state-of-the-art OER catalysts, which account for approximately 25% of the total cost of a PEM electrolyzer.[4,5] Consequently, there is a pressing need to reduce or even completely phase out noble metal usage while preserving high OER activity.[6,7] Co_3O_4 stands out as a promising alternative due to its affordability, relative stability, and considerable catalytic activity.[8−10]

Co_3O_4 is characterized by its spinel structure (AB_2O_4), which features adjustable mixed-valence states of Co^{3+} and Co^{2+}.[11−13] The dynamic between Co^{2+} and Co^{3+} within this framework as well as their spatial arrangement on various crystal facets plays a crucial role in its catalytic efficacy. This opens up new avenues for the development of high-performance cobalt-based catalysts. Koel et al. demonstrated that Co^{3+} on (111) facets exhibits superior OER activity compared to (100) facets in alkaline electrolytes.[14] Ding et al. also pointed out that the OER performance of Co_3O_4 {112} and {110} facets is much better than that of {100}.[15] These findings underscore that the ratio and distribution of Co^{2+} and Co^{3+} across crystal facets are directly correlated with the OER activity. Despite these progresses, there is still limited research on the OER performance of different Co_3O_4 crystal facets in acidic environments. It should be noted that the facets with high reactivity may also promote corrosion in acidic media, leading to inferior stability. However, the facet-dependent OER activity and Co_3O_4 corrosion have not been thoroughly studied.

To further enhance the performance of cobalt-based catalysts, researchers have explored various modification strategies, including defect engineering,[16] morphology control,[17] and elemental doping.[9] Among these, doping with transition metals such as ruthenium (Ru) has proven to be an

Received: June 30, 2024
Revised: September 4, 2024
Accepted: September 6, 2024
Published: September 12, 2024

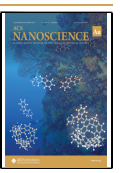

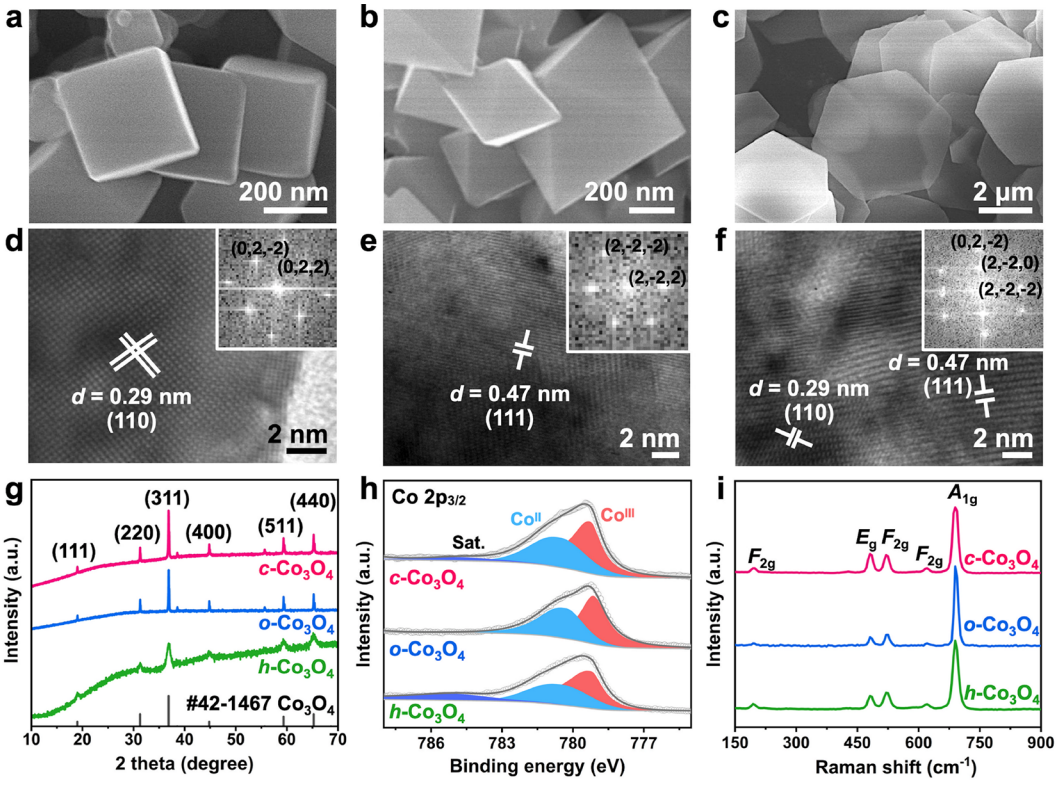

Figure 1. Structural characterization of Co_3O_4 catalysts. (a–c) SEM and (d–f) HRTEM images (insets of d–f are the corresponding FFT images), (g) XRD patterns, (h) Co $2p_{3/2}$ XPS spectra, and (i) Raman spectra of *c*-Co_3O_4, *o*-Co_3O_4, and *h*-Co_3O_4.

effective approach to enhance the OER performance.[18,19] Ru doping not only optimizes the electronic structure and increases the number of active sites but also improves charge transfer efficiency, enhances atom utilization, and boosts the OER performance of the catalyst. Our previous study demonstrated that through cation exchange, Ru^{3+} can replace the octahedral Co^{3+} sites in Co_3O_4, significantly enhancing both the OER activity and stability.[20]

Based on these findings, we synthesized spinel Co_3O_4 catalysts with different exposed crystal facets to investigate the impact of cobalt geometric sites on the electrocatalytic activity and stability. The results demonstrated that *h*-Co_3O_4, with mixed {111} and {110} crystal facets, exhibited a higher OER activity due to its higher Co^{3+} content. However, the abundance of Co^{3+} also led to deactivation of the catalyst over time due to the generation of soluble CoO_2. To address this issue, we further incorporated Ru into the best-performing Co_3O_4 to modify the electronic structure and thus the electrochemical behavior. The resulting Co_3O_4/RuO_2 heterostructure exhibits an overpotential of 257 mV at 10 mA cm^{-2} and can stably catalyze the OER for 100 h, representing an order of magnitude improvement in stability compared to the unmodified catalyst.

2. MATERIALS AND METHODS

2.1. Materials

Cobalt nitrate [$Co(NO_3)_2{\cdot}6H_2O$], cobalt acetate [$Co(CH_3COO)_2{\cdot}4H_2O$], perchloric acid ($HClO_4$), sulfuric acid ($H_2SO_4$), ethyl alcohol ($C_2H_5OH$), isopropyl alcohol ($CH_3CHOHCH_3$), acetone ($CH_3OCH_3$), and nitric acid ($HNO_3$) were purchased from Sinopharm Chemical Reagent Co., Ltd. Ruthenium chloride hydrate ($RuCl_3{\cdot}xH_2O$, 37% Ru basis) and commercial ruthenium dioxide (RuO_2) were purchased from Shanghai Aladdin Biochemical Co., Ltd. Carbon paper (thickness: 2 mm) and 5 wt % Nafion were purchased from Suzhou Sinero Technology Co. All chemicals (analytical grade) were used without further purification.

2.2. Preparation of Co_3O_4 with Different Crystal Facets

2.2.1. Synthesis of Co_3O_4 Nanocubes (*c*-Co_3O_4). 80 mmol of $Co(NO_3)_2{\cdot}6H_2O$ and 20 mmol of NaOH were dissolved in 80 mL of deionized water. The above mixture was then transferred to a Teflon stainless steel hydrothermal reactor, which was then sealed and placed in a 180 °C blast oven for 5 h. After the reaction stops, the product was centrifuged, washed twice with deionized water and once with ethanol, and then dried overnight in a 60 °C oven. Finally, the dried black powder was calcined for 4 h in a tube furnace or Muffle furnace under an air atmosphere at a calcination temperature of 500 °C and a heating rate of 5 °C min^{-1} to obtain *c*-Co_3O_4.

2.2.2. Synthesis of Co_3O_4 Octahedra (*o*-Co_3O_4). The process is similar to that of *c*-Co_3O_4, except that the concentrations of $Co(NO_3)_2{\cdot}6H_2O$ and NaOH were adjusted to 400 and 20 mmol, respectively.

2.2.3. Synthesis of Co_3O_4 Hexagonal Nanoplates (*h*-Co_3O_4). 0.25g $CH_3COO)_2Co{\cdot}4H_2O$ was dissolved in 18 mL of glycol and then transferred into a 25 mL Teflon stainless steel hydrothermal reactor. After sealing, it was placed in a blast oven at 200 °C for 12 h. After the reaction, the product was centrifuged, washed using deionized water, and ethanol, and then dried overnight in a 60 °C oven. Finally, the dried pink powder was calcined for 3 h in a tube furnace under an air atmosphere; the calcination temperature was 350 °C, and the heating rate was 5 °C min^{-1}.

2.3. Preparation of Co_3O_4/RuO_2

The Co_3O_4/RuO_2 was synthesized by cation exchange followed by thermal calcination. Specifically, the *h*-Co_3O_4 grown on a carbon cloth substrate was soaked in a $RuCl_3$ aqueous solution under 60 °C, and then rinsed with deionized water, dried, and finally calcined at 350 °C for 3 h under an air atmosphere. The heating rate was 5 °C min^{-1}. The contents of Ru and Co were determined by an inductively

https://doi.org/10.1021/acsnanoscienceau.4c00037
ACS Nanosci. Au 2024, 4, 409–415

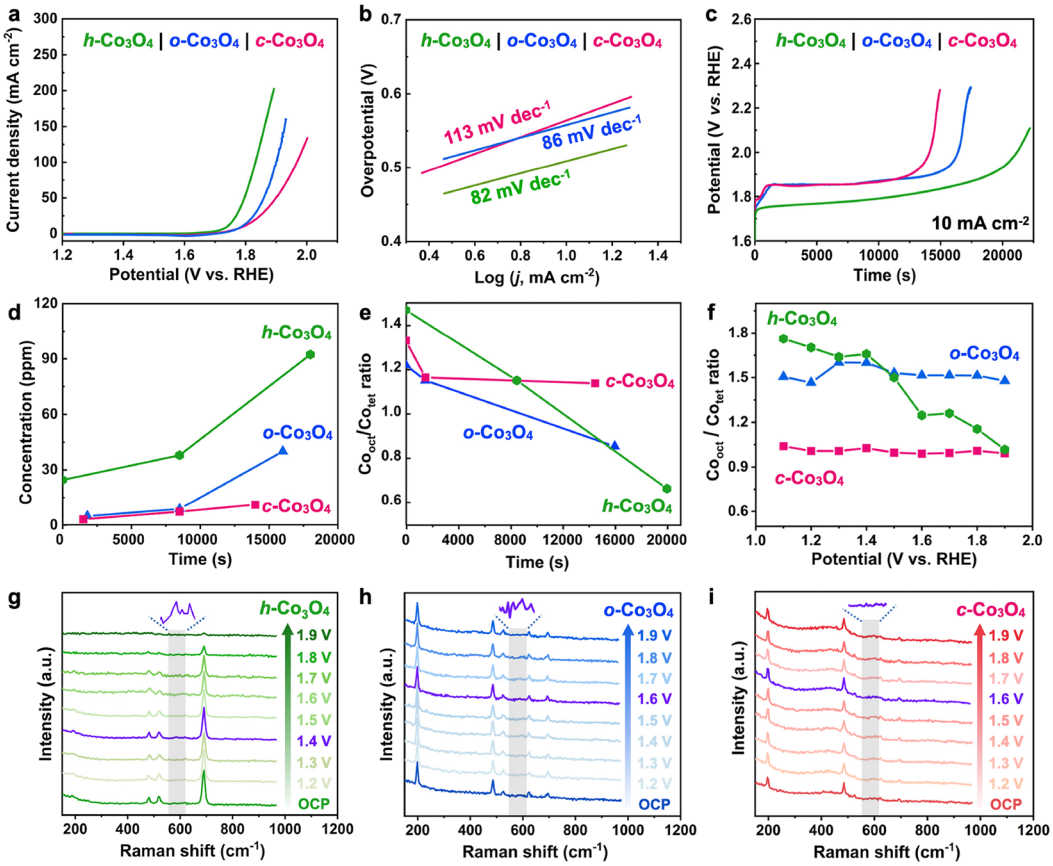

Figure 2. Electrochemical characterization of the three Co_3O_4 catalysts. (a) LSV curves, (b) Tafel plots, and (c) chronopotentiometry curves. (d) Cobalt dissolution during the stability test as monitored using ICP-MS. (e) Changes in the Co^{3+}/Co^{2+} ratio as measured by XPS. (f) Changes in Co^{3+}/Co^{2+} as measured by *in situ* Raman. (g, h) *In situ* Raman spectra under applied potentials of the *h*-Co_3O_4, *c*-Co_3O_4, and *o*-Co_3O_4.

coupled plasma optical emission spectrometer (ICP-OES) at 0.55 and 2.64 mg cm^{-2}, respectively.

2.4. Preparation of Electrodes

2 mg of catalyst (Co_3O_4 or RuO_2), 100 μL of isopropyl alcohol, and 10 μL of 5 wt % Nafion were dispersed in 100 μL of deionized water. After the catalyst was completely dispersed into a stable suspension by ultrasound for 40 min, it was evenly coated on the pretreated carbon paper and then dried using an infrared lamp.

2.5. Characterization

X-ray diffraction (XRD) patterns of Cu Kα radiation (λ = 1.5405 Å) in the 2 theta range of 10−70 were recorded by a Rigaku Ultima IV XRD diffractometer. Scanning electron microscopy (SEM) images were collected by using a Hitachi S-4800 microscope. Transmission electron microscopy (TEM) and high-angle annular dark-field scanning TEM (HAADF-STEM) images were recorded on an FEI Tecnai F30 at an acceleration voltage of 300 kV. X-ray photoelectron spectroscopy (XPS) analysis was conducted on a Thermo Scientific ESCALAB 250Xi spectroscope with Al Kα radiation. Raman spectra were obtained using a Renishaw inVia confocal Raman microscope under the excitation of a 4.0 mW, 532 nm laser. The *in situ* Raman tests were conducted in 0.5 M H_2SO_4 using AgCl/Ag as the reference electrode, wherein the potentials were not corrected for iR_s compensation. The mass loading of materials and the rate of metal dissolution were measured by an Agilent 7700 ICP-MS spectrometer.

2.6. Electrochemical Test

OER electrocatalysis was performed at room temperature using a standard three-electrode system in 0.5 M H_2SO_4 using a CHI 660E workstation. The catalyst was used as the working electrode, a Pt sheet was used as the counter electrode, and Hg/Hg_2SO_4 was used as the reference electrode. Linear sweep voltammetry (LSV) curves were recorded at a scanning rate of 5 mV s^{-1}. All the potentials reported in this work were corrected by ohmic loss unless otherwise specified except for the *in situ* Raman spectra. R_s was obtained by electrochemical impedance spectroscopy (EIS) measurement. Chronopotentiometry measurements were conducted at a benchmark current density of 10 mA cm^{-2}. The metal dissolution in the electrolyte was monitored by ICP-MS.

3. RESULTS AND DISCUSSION

We synthesized spinel Co_3O_4 nanocrystals with distinct morphologies, specifically nanocubes (*c*-Co_3O_4), octahedra (*o*-Co_3O_4), and hexagonal nanoplates (*h*-Co_3O_4), using reported methods.[21] The morphology of the prepared samples was investigated by SEM and TEM. The result (Figure 1a−f) reveals that *c*-Co_3O_4 exhibits a well-defined cubic structure with six {100} facets, and *o*-Co_3O_4 consists of octahedra with eight {111} facets, while for the *h*-Co_3O_4, although the SEM image indicates its well-structured plate-like morphology, TEM observation clearly suggests that the nanoplates are in fact an assembly of many nanoparticles (Figure S1). The main exposed facets of these particles were further determined to be {111} and {220} facets. The structures of the three Co_3O_4 samples were further characterized using XRD. The result (Figure 1g) reveals that the diffraction patterns of all three samples match well with pure spinel Co_3O_4, and no impurities are observed. XPS spectra of Co $2p_{3/2}$ can be fitted into Co^{3+} and Co^{2+} components, with binding energies at 779.4 and 780.8 eV, respectively (Figure 1h). Further analysis reveals that *h*-Co_3O_4 has the highest surface Co^{3+}/Co^{2+} ratio, followed by

https://doi.org/10.1021/acsnanoscienceau.4c00037
ACS Nanosci. Au 2024, 4, 409−415

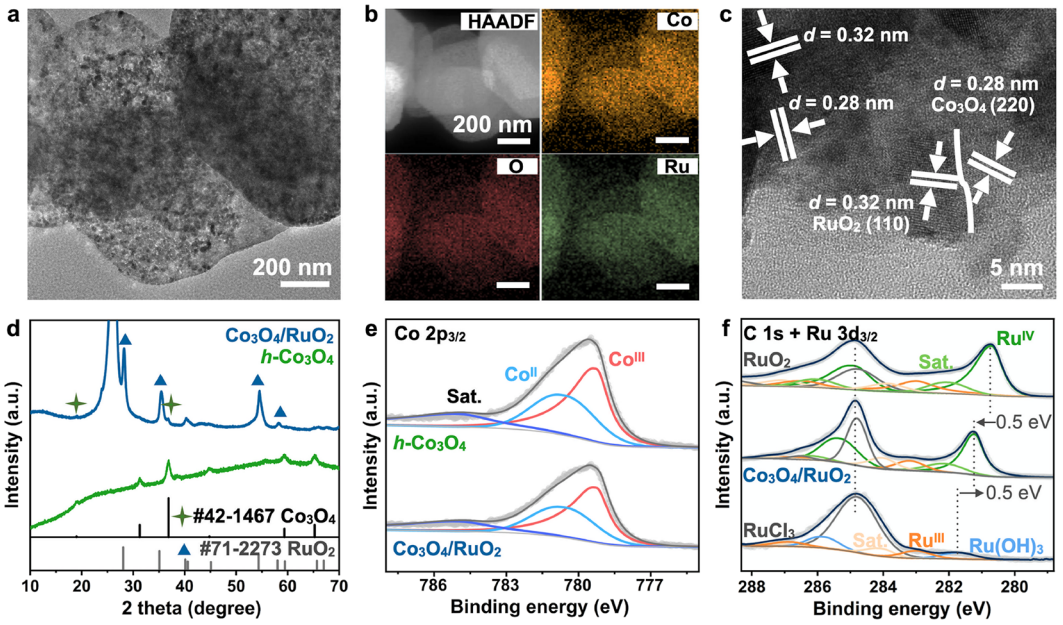

Figure 3. Structural characterization of Co_3O_4/RuO_2. (a) TEM image. (b) HAADF image and the corresponding elemental maps. (c) HRTEM image. (d) XRD patterns. (e) Co $2p_{3/2}$ and (f) Ru $3d_{3/2}$ XPS spectra.

o-Co_3O_4 and then *o*-Co_3O_4 (Table S1). This could be attributed to a surface atomic arrangement that ensures a high Co^{3+} density (Figure S2). We further conducted Raman analysis (Figure 1i). The vibrational modes at 198, 486, 523, and 693 cm^{-1} correspond to the F_{2g}, E_g, and A_{1g} modes of spinel Co_3O_4, respectively, whereas the modes at 198 and 693 cm^{-1} correspond to the stretching vibrations of Co^{2+}-O in the tetrahedral CoO_4 units and Co^{3+}-O in the octahedral CoO_6 units, respectively.[22,23] The intensity ratio of these peaks to the E_g peak reflects the relative surface content of Co^{2+} and Co^{3+} species. The result indicates that the Co^{3+}/Co^{2+} ratio follows the order *h*-Co_3O_4 > *o*-Co_3O_4 > *c*-Co_3O_4 (Table S2), consistent with the XPS result. It has been reported that Co^{3+} is the primary active site for the OER,[12,13,24] suggesting that *h*-Co_3O_4 is likely to exhibit higher OER activity.

The OER performance of Co_3O_4 with different exposed crystal facets was then studied in 0.5 M H_2SO_4. LSV curves indicate that *h*-Co_3O_4 exhibits the best OER activity among the three samples, with an overpotential of 500 mV at 10 mA cm^{-2}, followed by *o*-Co_3O_4 (557 mV) and *c*-Co_3O_4 (565 mV). The Tafel plots (Figure 2b) further verify the distinct OER activity of these three catalysts, with *h*-Co_3O_4 exhibiting the lowest Tafel slope of 82.52 mV dec^{-1}. This result confirms that a higher surface Co^{3+} ratio would result in higher apparent OER activity. The stability of these catalysts was further evaluated using a chronoamperometric test (Figure 2f). Interestingly, the result reveals that *h*-Co_3O_4 also has a higher stability at a current density of 10 mA cm^{-2}. However, it is also noted that the potential of *h*-Co_3O_4 increased slowly but continuously in the initial phase before stabilizing, while the potentials of *o*-Co_3O_4 and *c*-Co_3O_4 stabilized quickly after a quick rise. The morphology of the three catalysts after the OER remains largely unchanged (Figure S3). The sharp decrease in catalytic activity without significant morphological changes may be attributed to the deactivation of active sites at the catalytic interface during repeated electrochemical cycles. This deactivation could result from the accumulation of adsorbed molecules, charge rearrangement, or local variations around the active centers.[25] According to the previous discussion, the content of Co^{3+} in *h*-Co_3O_4 is the highest; however, ICP-MS analysis of cobalt dissolution during the OER process reveals that *h*-Co_3O_4 also exhibits the fastest cobalt dissolution rate (Figure 2d), while *o*-Co_3O_4 and *c*-Co_3O_4 show relatively lower levels. XPS analysis further shows a significant decrease in the Co^{3+}/Co^{2+} ratio for *h*-Co_3O_4 (Figure S4). This indicates that Co^{3+} at octahedral sites is more active for the OER, but a high Co^{3+} content also accelerates cobalt dissolution during the OER process (Figure 2e). This was further verified by the evolution of the Co^{3+}/Co^{2+} ratio of the three catalysts based on *in situ* Raman analysis (Figure 2f). *h*-Co_3O_4 shows a constant decrease in the Co^{3+} ratio during the OER. Note that the ratio of Co^{3+}/Co^{2+} determined by Raman is slightly higher than that determined by XPS, which might be because the former is bulk sensitive while the latter is mostly surface sensitive. The *in situ* Raman spectra collected during the OER further reveal that as the potential increases, a vibrational peak associated with CoO_2 appears at around 578 cm^{-1}.[26] For *h*-Co_3O_4, this peak of CoO_2 emerged at a relatively low potential of 1.4 V (Figure 2g) due to the high Co^{3+} content, and it disappeared at higher potentials as CoO_2 readily dissolves in acidic conditions. In contrast, *o*-Co_3O_4 exhibited the CoO_2 peak at a higher potential of 1.6 V, likely due to its lower surface Co^{3+} content (Figure 2h). Although no distinct peak was observed for *c*-Co_3O_4 at 1.6 V, the absence of the adjacent 620 cm^{-1} peak indicates the formation of CoO_2 (Figure 2i). The above results indicate that the Co^{3+} species play important roles in determining both the OER activity and the stability. On the one hand, the presence of abundant Co^{3+} species promotes the generation of the highly active CoO_2 phase, contributing to the high OER activity. On the other hand, the generated CoO_2 would easily dissolve in acidic electrolytes, leading to the loss of active materials and consequently performance decay. These two factors would result in the activity−stability trade-off effect of the Co_3O_4 catalyst. However, it is surprising that although *h*-Co_3O_4 has the fastest Co dissolution rate, it shows the best

https://doi.org/10.1021/acsnanoscienceau.4c00037
ACS Nanosci. Au 2024, 4, 409−415

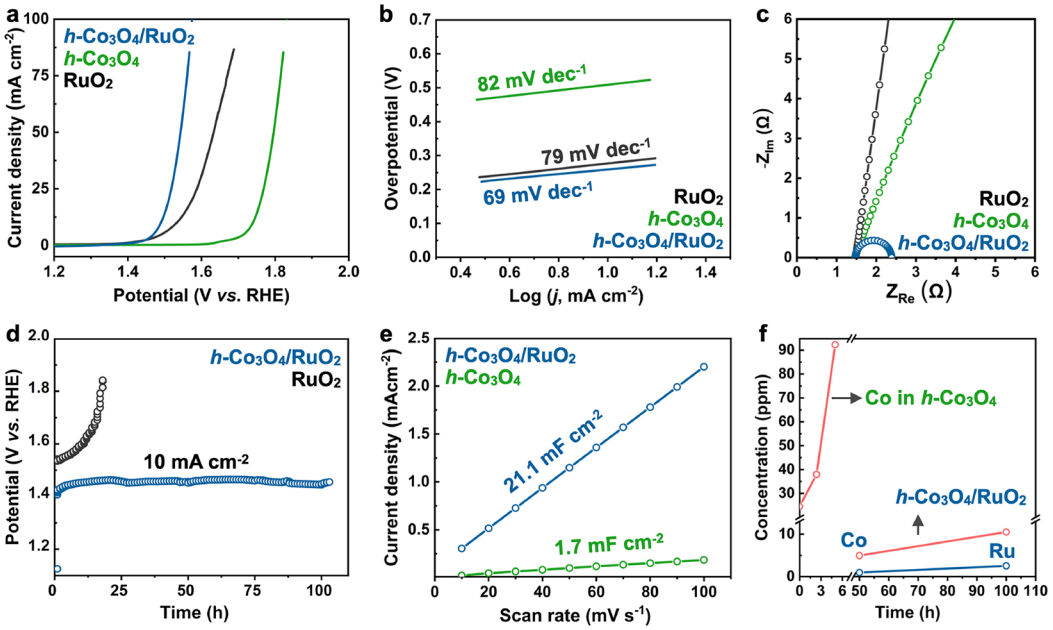

Figure 4. Acidic OER performance of h-Co_3O_4/RuO_2. (a) LSV curves. (b) Tafel plots. (c) EIS spectra. (d) Chronopotentiometry curve. (e) Calculated specific C_{dl} plots. (f) Metal dissolution during the stability test.

durability (Figure 2c). This might be due to the high surface Co^{3+} density that could sustain a relatively long dissolution, although further investigation is required.

The above result suggests that h-Co_3O_4 has better OER activity and stability against o-Co_3O_4 and c-Co_3O_4. We then employed h-Co_3O_4 as the support to incorporate Ru atoms to further enhance the OER performance (see the detailed synthesis procedure in the Supporting Information). The resulting catalyst inherits the hexagonal plate-like morphology (Figure 3a). The HAADF image and the corresponding elemental mapping further confirm the successful incorporation of Ru (Figure 4b), and the Ru content was determined to be only 2.42 wt %. The HRTEM image reveals an interface between the (220) facet of Co_3O_4 and the (110) facet of RuO_2 (Figure 4c), indicating the formation of a Co_3O_4/RuO_2 heterostructure. Indeed, the XRD patterns further confirm the presence of both Co_3O_4 and RuO_2 (Figure 4d). Note that the strong diffraction peak at around 26.5° is a characteristic peak of the carbon paper substrate (Figure S5). To identify the possible electronic interactions between the Co and Ru species, we conducted the XPS analysis. Compared with h-Co_3O_4, the Co^{3+}/Co^{2+} ratio in Co_3O_4/RuO_2 decreases, indicating that some Ru atoms occupy Co^{3+} sites in h-Co_3O_4 (Figure 3e). The Ru 3d spectra shows that the binding energy of Ru 3p in Co_3O_4/RuO_2 is higher than that in RuO_2 but lower than in $RuCl_3$ (Figure 3f), suggesting that the oxidation state of Ru in the synthesized catalyst lies between +3 and +4.[27] This confirms that Ru doping in h-Co_3O_4 can modulate the electronic distribution and coordination environment.

Subsequently, the OER performance of h-Co_3O_4/RuO_2 was measured in 0.5 M H_2SO_4, revealing a significant enhancement in the activity. The catalyst requires an overpotential of only 257 mV to drive a current density of 10 mA cm^{-2} (Figure 4a), which is 243 mV lower than the pristine h-Co_3O_4 and superior to commercial RuO_2 (300 mV). Additionally, the OER kinetics are notably accelerated, as evidenced by a decrease in the Tafel slope from 82.52 to 69.82 mV dec^{-1} (Figure 4b). EIS measurement demonstrates that h-Co_3O_4/RuO_2 has the lowest charge transfer resistance (Figure 4c), further corroborating its excellent electrocatalytic activity and efficient charge transfer properties. h-Co_3O_4/RuO_2 also exhibits excellent stability that can stably drive the current density of 10 mA cm^{-2} for 100 h (Figure 4d). The potential increase is negligible compared to the initial potential, marking a significant stability improvement over that of pristine h-Co_3O_4 by an order of magnitude. With the incorporation of Ru, h-Co_3O_4/RuO_2 exhibits a significantly higher electrochemically active surface area (ECSA, Figure S6), soaring from 42.7 to 526.5 cm^2 (Figures 4e). At the same time, this remarkable increase not only underscores the success of the Ru doping strategy but also highlights its efficacy in increasing the number of active sites, thereby enhancing the catalytic efficiency. In strong acidic electrolytes, cobalt-based oxides exhibit a decline in activity during prolonged OER, with significant dissolution being a major cause of deactivation,[10] as confirmed by our above characterizations. During the testing of h-Co_3O_4/RuO_2, it was observed that the incorporation of Ru not only significantly suppresses the dissolution of cobalt but also maintains the Ru dissolution rate at a low level (Figure 4f). This could be attributed to the interactions between Ru and Co that suppress the overoxidation of Ru/Co species. In addition, it should be noted that the required potential at 10 mA cm^{-2} for h-Co_3O_4/RuO_2 (1.73 V vs RHE) is significantly lower than that for h-Co_3O_4 (1.48 V), which also contributes to the slower Co dissolution rate. We also synthesized o-Co_3O_4/RuO_2 and c-Co_3O_4/RuO_2 following the same recipe and measured the electrocatalytic OER performance (Figure S7). The result indicates that RuO_2 tends to accumulate on the surface rather than incorporate into the lattice, likely due to the dense surface of the Co_3O_4 octahedra and cubes. Although the as-obtained o-Co_3O_4/RuO_2 and c-Co_3O_4/RuO_2 both show improved OER activity and stability, the enhancement is much less significant compared to h-Co_3O_4/RuO_2. This result suggests that the incorporation of Ru^{3+} into the h-Co_3O_4 lattice contributes significantly to the high OER performance.

Post XRD analysis reveals that although the diffraction peaks of h-Co_3O_4 are no longer visible (Figure S8), the TEM

https://doi.org/10.1021/acsnanoscienceau.4c00037
ACS Nanosci. Au 2024, 4, 409−415

investigation shows that the morphology remains almost unchanged (Figure S9). XPS analysis further indicates that the valence state of Ru exhibits negligible changes, suggesting the stability of RuO_2 in the h-Co_3O_4/RuO_2 heterostructure (Figure S10). The Co^{3+}/Co^{2+} ratio in h-Co_3O_4/RuO_2 decreases slightly from 1.42 to 1.15 after the test due to the dissolution of Co during the stability process. This supports the idea that Co^{3+} in h-Co_3O_4 oxidizes to soluble CoO_2 in the heterojunction. The significant increase in oxygen vacancies after the test may indicate the coexistence of the adsorbate evolution mechanism (AEM) and lattice oxygen mechanism (LOM) during the OER process, and the LOM contributes to the formation of additional oxygen vacancies and leads to the irreversible dissolution of Co_3O_4.[28] These findings indicate that h-Co_3O_4/RuO_2 exhibits superior corrosion resistance in highly acidic environments, meeting the demands for long-term operation.

4. CONCLUSIONS

In summary, we systematically investigated the differences in the acidic OER performance of Co_3O_4 exposing three distinct crystal planes. Electrochemical tests indicate that h-Co_3O_4, exposing mixed {111} and {110} planes, exhibits the highest OER activity and stability, which could serve as an ideal support to load Ru. We further synthesized Co_3O_4/RuO_2 heterostructures, which require an overpotential of only 257 mV at an OER current density of 10 mA cm^{-2} and could stably catalyze the OER over 100 h at this current density, achieving an order-of-magnitude improvement in stability compared to pure Co_3O_4. The significant enhancement in catalytic activity is attributed to Ru substituting part of the octahedral Co coordination, thereby inhibiting Co dissolution and providing high-activity sites. This Ru doping strategy might be extended to other transition metal oxide catalysts beyond cobalt oxides.

ASSOCIATED CONTENT

Supporting Information

The Supporting Information is available free of charge at https://pubs.acs.org/doi/10.1021/acsnanoscienceau.4c00037.

Additional SEM, TEM figures, and electrochemical data (PDF)

AUTHOR INFORMATION

Corresponding Author

Hanfeng Liang − *State Key Laboratory of Physical Chemistry of Solid Surfaces, College of Chemistry and Chemical Engineering, Xiamen University, Xiamen 361005, China;* orcid.org/0000-0002-1778-3975; Email: hfliang@xmu.edu.cn

Author

Mengting Zhao − *State Key Laboratory of Physical Chemistry of Solid Surfaces, College of Chemistry and Chemical Engineering, Xiamen University, Xiamen 361005, China*

Complete contact information is available at: https://pubs.acs.org/10.1021/acsnanoscienceau.4c00037

Notes

The authors declare no competing financial interest.

ACKNOWLEDGMENTS

This work was supported by the Fundamental Research Funds for the Central Universities, China (20720240066).

REFERENCES

(1) Carmo, M.; Fritz, D. L.; Mergel, J.; Stolten, D. A Comprehensive Review on Pem Water Electrolysis. *Int. J. Hydrogen Energy* **2013**, *38* (12), 4901−4934.

(2) Seh, Z. W.; Kibsgaard, J.; Dickens, C. F.; Chorkendorff, I.; Nørskov, J. K.; Jaramillo, T. F. Combining Theory and Experiment in Electrocatalysis: Insights into Materials Design. *Science* **2017**, *355* (6321), No. eaad4998.

(3) Zhu, W.; Huang, Z.; Zhao, M.; Huang, R.; Wang, Z.; Liang, H. Hydrogen Production by Electrocatalysis Using the Reaction of Acidic Oxygen Evolution: A Review. *Environ. Chem. Lett.* **2022**, *20* (6), 3429−3452.

(4) Lin, Y.; Dong, Y.; Wang, X.; Chen, L. Electrocatalysts for the Oxygen Evolution Reaction in Acidic Media. *Adv. Mater.* **2023**, *35* (22), No. 2210565.

(5) Geiger, S.; Kasian, O.; Shrestha, B. R.; Mingers, A. M.; Mayrhofer, K. J. J.; Cherevko, S. Activity and Stability of Electrochemically and Thermally Treated Iridium for the Oxygen Evolution Reaction. *J. Electrochem. Soc.* **2016**, *163* (11), F3132.

(6) Xiong, X.; Tang, J.; Ji, Y.; Xue, W.; Wang, H.; Liu, C.; Zeng, H.; Dai, Y.; Peng, H.; Zheng, T.; Xia, C.; Liu, X.; Jiang, Q. High-Efficiency Iridium-Yttrium Alloy Catalyst for Acidic Water Electrolysis. *Adv. Energy Mater.* **2024**, *14* (20), No. 2304479.

(7) Liang, H.; Cao, Z.; Xia, C.; Ming, F.; Zhang, W.; Emwas, A.-H.; Cavallo, L.; Alshareef, H. N. Tungsten Blue Oxide as a Reusable Electrocatalyst for Acidic Water Oxidation by Plasma-Induced Vacancy Engineering. *CCS Chem.* **2021**, *3* (3), 1553−1561.

(8) Gao, J.; Tao, H.; Liu, B. Progress of Nonprecious-Metal-Based Electrocatalysts for Oxygen Evolution in Acidic Media. *Adv. Mater.* **2021**, *33* (31), No. 2003786.

(9) Li, A.; Kong, S.; Guo, C.; Ooka, H.; Adachi, K.; Hashizume, D.; Jiang, Q.; Han, H.; Xiao, J.; Nakamura, R. Enhancing the Stability of Cobalt Spinel Oxide Towards Sustainable Oxygen Evolution in Acid. *Nat. Catal.* **2022**, *5* (2), 109−118.

(10) Mondschein, J. S.; Callejas, J. F.; Read, C. G.; Chen, J. Y. C.; Holder, C. F.; Badding, C. K.; Schaak, R. E. Crystalline Cobalt Oxide Films for Sustained Electrocatalytic Oxygen Evolution under Strongly Acidic Conditions. *Chem. Mater.* **2017**, *29* (3), 950−957.

(11) Xu, Y.; Zhang, F.; Sheng, T.; Ye, T.; Yi, D.; Yang, Y.; Liu, S.; Wang, X.; Yao, J. Clarifying the Controversial Catalytic Active Sites of Co_3O_4 for the Oxygen Evolution Reaction. *J. Mater. Chem. A* **2019**, *7* (40), 23191−23198.

(12) An, L.; Zhang, H.; Zhu, J.; Xi, S.; Huang, B.; Sun, M.; Peng, Y.; Xi, P.; Yan, C.-H. Balancing Activity and Stability in Spinel Cobalt Oxides through Geometrical Sites Occupation Towards Efficient Electrocatalytic Oxygen Evolution. *Angew. Chem., Int. Ed.* **2023**, *62* (3), No. e202214600.

(13) Sun, S.; Sun, Y.; Zhou, Y.; Xi, S.; Ren, X.; Huang, B.; Liao, H.; Wang, L. P.; Du, Y.; Xu, Z. J. Shifting Oxygen Charge Towards Octahedral Metal: A Way to Promote Water Oxidation on Cobalt Spinel Oxides. *Angew. Chem., Int. Ed.* **2019**, *58* (18), 6042−6047.

(14) Chen, Z.; Kronawitter, C. X.; Koel, B. E. Facet-Dependent Activity and Stability of Co_3O_4 Nanocrystals Towards the Oxygen Evolution Reaction. *Phys. Chem. Chem. Phys.* **2015**, *17* (43), 29387−29393.

(15) Zhou, X.; Liu, Z.; Wang, Y.; Ding, Y. Facet Effect of Co_3O_4 Nanocrystals on Visible-Light Driven Water Oxidation. *Appl. Catal., B* **2018**, *237*, 74−84.

(16) Zhang, R.; Pan, L.; Guo, B.; Huang, Z. F.; Chen, Z.; Wang, L.; Zhang, X.; Guo, Z.; Xu, W.; Loh, K. P.; Zou, J. J. Tracking the Role of Defect Types in Co_3O_4 Structural Evolution and Active Motifs During Oxygen Evolution Reaction. *J. Am. Chem. Soc.* **2023**, *145* (4), 2271−2281.

(17) Ortiz Peña, N.; Ihiawakrim, D.; Han, M.; Lassalle-Kaiser, B.; Carenco, S.; Sanchez, C.; Laberty-Robert, C.; Portehault, D.; Ersen, O. Morphological and Structural Evolution of Co_3O_4 Nanoparticles Revealed by in Situ Electrochemical Transmission Electron Microscopy During Electrocatalytic Water Oxidation. *ACS Nano* **2019**, *13* (10), 11372−11381.
(18) Deng, L.; Liu, S.; Liu, D.; Chang, Y. M.; Li, L.; Li, C.; Sun, Y.; Hu, F.; Chen, H. Y.; Pan, H.; Peng, S. Activity-Stability Balance: The Role of Electron Supply Effect of Support in Acidic Oxygen Evolution. *Small* **2023**, *19* (30), No. e2302238.
(19) Liu, Z.; Zeng, L.; Yu, J.; Yang, L.; Zhang, J.; Zhang, X.; Han, F.; Zhao, L.; Li, X.; Liu, H.; Zhou, W. Charge Redistribution of Ru Nanoclusters on Co_3O_4 Porous Nanowire Via the Oxygen Regulation for Enhanced Hydrogen Evolution Reaction. *Nano Energy* **2021**, *85*, No. 105940.
(20) Zhu, W.; Yao, F.; Cheng, K.; Zhao, M.; Yang, C.-J.; Dong, C.-L.; Hong, Q.; Jiang, Q.; Wang, Z.; Liang, H. Direct Dioxygen Radical Coupling Driven by Octahedral Ruthenium−Oxygen−Cobalt Collaborative Coordination for Acidic Oxygen Evolution Reaction. *J. Am. Chem. Soc.* **2023**, *145* (32), 17995−18006.
(21) Zhai, G.; Wang, J.; Chen, Z.; An, W.; Men, Y. Boosting Soot Combustion Efficiency of Co_3O_4 Nanocrystals Via Tailoring Crystal Facets. *Chem. Eng. J.* **2018**, *337*, 488−498.
(22) Hadjiev, V. G.; Iliev, M. N.; Vergilov, I. V. The Raman Spectra of Co_3O_4. *J. Phys. C: Solid State Phys.* **1988**, *21* (7), L199.
(23) Ravina; Dalela, S.; Kumar, S.; Choudhary, B. L.; Alvi, P. A. Structural, Optical and Raman Studies of Co_3O_4 Nano-Particles. *Mater. Today: Proc.* **2023**, *79*, 165−168.
(24) Liu, Z.; Wang, G.; Zhu, X.; Wang, Y.; Zou, Y.; Zang, S.; Wang, S. Optimal Geometrical Configuration of Cobalt Cations in Spinel Oxides to Promote Oxygen Evolution Reaction. *Angew. Chem., Int. Ed.* **2020**, *59* (12), 4736−4742.
(25) Chen, F.-Y.; Wu, Z.-Y.; Adler, Z.; Wang, H. Stability Challenges of Electrocatalytic Oxygen Evolution Reaction: From Mechanistic Understanding to Reactor Design. *Joule* **2021**, *5* (7), 1704−1731.
(26) Natarajan, K.; Munirathinam, E.; Yang, T. C. K. Operando Investigation of Structural and Chemical Origin of Co_3O_4 Stability in Acid under Oxygen Evolution Reaction. *ACS Appl. Mater. Interfaces* **2021**, *13* (23), 27140−27148.
(27) Morgan, D. J. Resolving Ruthenium: XPS Studies of Common Ruthenium Materials. *Surf. Interface Anal.* **2015**, *47* (11), 1072−1079.
(28) Huang, X.; Lee, C.; Li, Y.; Xu, J.; Liu, D. Acid-Treated RuO_2/Co_3O_4 Nanostructures for Acidic Oxygen Evolution Reaction Electrocatalysis. *ACS Appl. Nano Mater.* **2024**, *7* (8), 9244−9251.

https://doi.org/10.1021/acsnanoscienceau.4c00037
ACS Nanosci. Au 2024, 4, 409−415